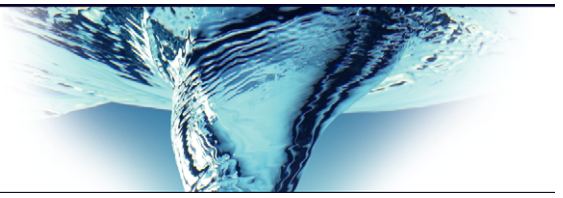
JFM RAPIDS
journals.cambridge.org/rapids



Stratified precessional flow in spherical geometry

Xing Wei† and Andreas Tilgner

Institute of Geophysics, University of Göttingen, Friedrich-Hund-Platz 1, 37077 Göttingen, Germany

(Received 8 August 2012; revised 27 January 2013; accepted 28 January 2013;
first published online 8 February 2013)

We investigate numerically, in spherical geometry, the interaction of stratification with precession. Both stable stratification and unstable stratification are studied. In the parameter regime we are concerned with, stable stratification suppresses the precessional instability, whereas unstable stratification and precession can either stabilize or destabilize each other at different precession rates.

Key words: geophysical and geological flows, rotating flows, stratified flows

1. Introduction and motivation

The magnetic field of many celestial bodies is maintained by the dynamo effect, which requires that the body contains a fluid conductor executing a non-trivial motion. The energy source for this motion is frequently assumed to be thermal convection. Accordingly, convection-driven dynamos in spherical spheres have been extensively studied (Busse 2000; Roberts & Glatzmaier 2000; Wicht & Tilgner 2010; Jones 2011). Bullard (1949) was the first to point out that precession is a possible energy source for the geodynamo. Precession-driven flows, their stability and dynamo properties have been investigated independently of thermal convection (Poincaré 1910; Busse 1968; Malkus 1968; Vanyo & Likins 1971; Tilgner 1999*a*; Noir *et al.* 2001; Tilgner & Busse 2001; Lorenzani & Tilgner 2001, 2003; Tilgner 2005). More recently, some attention has also been paid to other types of mechanical forcing, such as tides, libration and collisions (Weiss *et al.* 2008; Dwyer, Stevenson & Nimmo 2011; Le Bars *et al.* 2011).

For the Earth and the other planets and moons of the Solar System, mechanical forcing is well known, while it is uncertain if their cores are convecting. In general, it will always be necessary to consider buoyancy and a mechanical forcing such as precession in conjunction. The thermal stratification can be either unstable or stable depending on which epoch in the thermal history of a celestial body is being considered. Typically, the surface cooling of a recently formed body leads to a super-adiabatic gradient. As the heat generated during accretion and formation of

† Email address for correspondence: Xing.Wei@phys.uni-goettingen.de

doi:10.1017/jfm.2013.68

https://doi.org/10.1017/jfm.2013.68 Published online by Cambridge University Press

the body is progressively lost, the internal temperature gradient eventually drops below the adiabatic gradient, yielding a stable thermal stratification. Small bodies such as planetesimals or the Moon have already reached this point in the past.

In this paper, we investigate the hydrodynamics of stably and unstably stratified fluid in a precessing spherical shell. This is intended as a model of the Earth, whose precession is maintained by the gravitational torques of the Moon and the Sun, but also as a model of planetesimals in the early Solar System, which undergo force-free precessional motion after collisions if the direction of their angular momentum does not coincide with one of their principal axes of inertia.

In § 2 we formulate the problem and introduce the numerical methods. In § 3 we investigate the interaction of stable stratification and precession. In § 4 we investigate the interaction of unstable stratification and precession. We conclude with some discussion in § 5.

2. Equations and numerical methods

We consider a fluid in a spherical shell of inner radius r_i and outer radius r_o. Suppose that the spherical shell spins at the angular velocity $\boldsymbol{\Omega}_s$ and precesses at the angular velocity $\boldsymbol{\Omega}_p$. A background temperature T_b is imposed on the fluid, which we assume to be a linear function of radius,

$$T_b = \frac{T_o - T_i}{d}(r - r_o) + T_o, \tag{2.1}$$

where T_i and T_o are the temperature at r_i and r_o, respectively, and $d = r_o - r_i$ is the thickness of the gap. Such a background temperature is maintained by a heat source or sink that varies inversely proportional to radius (because $\nabla^2 T_b = 2(T_o - T_i)/rd$). An alternative model in which the stratification is imposed by fixed temperatures at the boundaries in the absence of a heat source leads to a non-uniform stratification and has not been considered for simplicity. In the frame moving with the boundary, the dimensional Navier–Stokes equation of a Boussinesq fluid reads

$$\begin{aligned}&\frac{\partial \boldsymbol{u}}{\partial t} + \boldsymbol{u}\cdot\boldsymbol{\nabla}\boldsymbol{u} + \boldsymbol{\Omega}_{ref}\times(\boldsymbol{\Omega}_{ref}\times\boldsymbol{r}) + 2\boldsymbol{\Omega}_{ref}\times\boldsymbol{u} + (\boldsymbol{\Omega}_p\times\boldsymbol{\Omega}_s)\times\boldsymbol{r}\\ &\quad = -\frac{1}{\rho_o}\boldsymbol{\nabla}p + \nu\nabla^2\boldsymbol{u} + \frac{\rho}{\rho_o}\boldsymbol{g}, \quad \boldsymbol{\nabla}\cdot\boldsymbol{u} = 0,\end{aligned} \tag{2.2}$$

where $\boldsymbol{\Omega}_{ref} = \boldsymbol{\Omega}_s + \boldsymbol{\Omega}_p$ is the angular velocity of the moving frame with respect to the inertial frame and ρ_o is the fluid density at r_o. In the Boussinesq approximation, density variations are only retained in the buoyancy term, and the density deviation is proportional to the temperature deviation,

$$\frac{\rho - \rho_o}{\rho_o} = -\alpha(T - T_o) = -\alpha(\Theta + T_b - T_o), \tag{2.3}$$

where $\Theta = T - T_b$ is the temperature deviation from the conductive profile and α is the thermal expansion. In a sphere of constant density, the gravitational acceleration is proportional to radius,

$$\boldsymbol{g} = -g_o\frac{\boldsymbol{r}}{r_o}, \tag{2.4}$$

where g_o is the gravity at r_o.

https://doi.org/10.1017/jfm.2013.68 Published online by Cambridge University Press

Substituting (2.3) and (2.4) into (2.2) and normalizing length with d, time with Ω_s^{-1}, $\boldsymbol{u}$ with $\Omega_s d$ and Θ with $(T_i - T_o)$, we obtain the dimensionless Navier–Stokes equation

$$\frac{\partial \boldsymbol{u}}{\partial t} + \boldsymbol{u}\cdot\boldsymbol{\nabla}\boldsymbol{u} = -\boldsymbol{\nabla}\Phi + Ek\nabla^2\boldsymbol{u} + 2\boldsymbol{u}\times(\hat{\boldsymbol{z}} + Po\widehat{\boldsymbol{\Omega}}_p) + Po(\hat{\boldsymbol{z}}\times\widehat{\boldsymbol{\Omega}}_p)\times\boldsymbol{r} + \widetilde{Ra}\Theta\boldsymbol{r}, \quad (2.5)$$

where all the curl-free terms, e.g. the centrifugal force and the term associated with T_b, are already absorbed into the total pressure Φ. In (2.5) there are three dimensionless parameters. The Ekman number,

$$Ek = \frac{\nu}{\Omega_s d^2}, \quad (2.6)$$

measures the ratio of the viscous time scale to the spin time scale. The Poincaré number,

$$Po = \frac{\Omega_p}{\Omega_s}, \quad (2.7)$$

measures the precession rate. Despite its unusual form, we choose to call the parameter in the buoyancy term the Rayleigh number,

$$\widetilde{Ra} = \frac{\alpha g_o (T_i - T_o)}{\Omega_s^2 r_o}, \quad (2.8)$$

which is proportional to the imposed stratification. A negative $\widetilde{Ra}$ corresponds to a stable stratification and a positive $\widetilde{Ra}$ to an unstable stratification. For a stable stratification, $\widetilde{Ra}$ is just the square of the dimensionless Brunt–Väisälä frequency. The unit vector along the precession axis in Cartesian coordinates (x, y, z) is

$$\widehat{\boldsymbol{\Omega}}_p = \sin\beta\cos t\,\hat{\boldsymbol{x}} - \sin\beta\sin t\,\hat{\boldsymbol{y}} + \cos\beta\,\hat{\boldsymbol{z}}, \quad (2.9)$$

where $\hat{\boldsymbol{z}}$ is the spin axis and β is the angle between the spin axis $\hat{\boldsymbol{z}}$ and the precession axis $\widehat{\boldsymbol{\Omega}}_p$. The boundary condition of velocity is no-slip at the outer boundary, whereas it is stress-free at the inner boundary to approximate a full sphere.

Accordingly, the dimensionless equation of temperature deviation is

$$\frac{\partial \Theta}{\partial t} + \boldsymbol{u}\cdot\boldsymbol{\nabla}\Theta - u_r = \frac{Ek}{Pr}\nabla^2\Theta. \quad (2.10)$$

In (2.10) the Prandtl number,

$$Pr = \frac{\nu}{\kappa}, \quad (2.11)$$

measures the ratio of viscosity to the thermal diffusivity. The boundary condition is $\Theta = 0$ at both inner and outer boundaries.

Equations (2.5) and (2.10) are solved numerically. In the calculations, we fix the aspect ratio r_i/r_o to 0.1, such that the spherical shell is almost a spherical cavity and hence the inner core is almost negligible, and the angle β to 60°. We investigate only retrograde precession ($Po < 0$), which is geophysically relevant. We fix the Prandtl number to $Pr = 1$. In the calculations of stable stratification, we fix $Po = -0.3$ and vary Ek and $\widetilde{Ra}$ to investigate how the stable stratification influences the precessional instability. In the calculations of unstable stratification, we select two Ekman numbers, $Ek = 5\times10^{-3}$ and 1×10^{-3}, which are sufficiently high to maintain

https://doi.org/10.1017/jfm.2013.68 Published online by Cambridge University Press

the flow precessionally stable, and vary Po and $\widetilde{Ra}$ to investigate the interaction of precessional and convective instabilities.

The numerical calculations are carried out in the spherical coordinates (r, θ, ϕ) with the parallel pseudo-spectral code provided by Tilgner (1999*b*). The toroidal–poloidal decomposition method is employed such that the divergence-free condition of fluid flow $\boldsymbol{\nabla} \cdot \boldsymbol{u} = 0$ is automatically satisfied. The spherical harmonics $P_l^m(\cos\theta)\mathrm{e}^{\mathrm{i}m\phi}$ are used on the spherical surface (θ, ϕ) and the Chebyshev polynomials $T_k(r)$ are used in the radial direction. Resolutions as high as 256 (radial r), 128 (colatitude θ) and 64 (longitude ϕ) are used. A semi-implicit scheme is employed for time stepping, using an Adams–Bashforth scheme for the nonlinear and a Crank–Nicolson scheme for the diffusive terms.

3. Stably stratified precessional flow

The precessional flow in the interior of a spherical container is mainly a solid-body rotation with angular velocity $\boldsymbol{\Omega}_f$, which is in general different from both $\boldsymbol{\Omega}_s$ and $\boldsymbol{\Omega}_p$ (Busse 1968). At the boundary, the fluid rotation matches the spin rate $\boldsymbol{\Omega}_s$ such that there exists an Ekman boundary layer, where the poloidal flow is generated by Ekman pumping. In addition to the boundary layers, there also exist internal shear layers that are spawned at the critical latitude (Tilgner 1999*a*). A well-understood instability mechanism in these flows is a triad resonance between the basic flow and two inertial modes (Kerswell 1995; Tilgner & Busse 2001; Lorenzani & Tilgner 2001, 2003).

We now consider the interaction of a stable stratification and precession. Radial stratification tends to suppress fluid motion in the radial direction, which suggests that stable stratification suppresses precessional instability. However, stable stratification leads to gravito-inertial waves whose frequencies may be closer to a perfect triad resonance than the pure inertial waves of the unstratified case, so that destabilization through stable stratification is possible too (Kerswell 1993). Only stabilization is observed in our numerical calculations. In the numerical calculations, we fix $Po = -0.3$ and calculate various combinations of Ek and $\widetilde{Ra}$, namely Ek ranges from 5×10^{-3} to 1×10^{-4} and $\widetilde{Ra}$ from 0 (purely precessional flow) to -1. Because a stable precessional flow is antisymmetric about the centre, i.e. $\boldsymbol{u}(-\boldsymbol{r}) = -\boldsymbol{u}(\boldsymbol{r})$, we use symmetries (Lorenzani & Tilgner 2001) to detect the precessional instability, i.e. the flow is separated into two parts, $\boldsymbol{u}_s(\boldsymbol{r}) = [\boldsymbol{u}(\boldsymbol{r}) - \boldsymbol{u}(-\boldsymbol{r})]/2$ and $\boldsymbol{u}_a(\boldsymbol{r}) = [\boldsymbol{u}(\boldsymbol{r}) + \boldsymbol{u}(-\boldsymbol{r})]/2$, and the kinetic energy of $\boldsymbol{u}_a$ represents the instability.

Figure 1 shows the total kinetic energy E (figure 1*a*) and the ratio of instability energy E_a to the total energy (figure 1*b*) against the Ekman number Ek at different Rayleigh numbers $\widetilde{Ra}$ (for time-dependent flows, E and E_a are calculated by averaging over time). Figure 1(*a*) shows that increasing Ek reduces the energy E. This behaviour is well known from previous studies and is due to the fact that the viscous term is more important at higher Ek, which damps any motion excited by the Poincaré force. It is also seen from figure 1(*a*) that a larger $|\widetilde{Ra}|$ reduces the energy. This is consistent with figure 2(*a*), which shows the modulus of the fluid rotation vector $|\boldsymbol{\omega}| = \sqrt{\omega_x^2 + \omega_y^2 + \omega_z^2}$ to indicate that a lower $|\widetilde{Ra}|$ corresponds to a stronger fluid rotation. In order to explain the data in figures 1(*a*) and 2, one would have to extend Busse's calculation (Busse 1968) to a stably stratified medium, which is not attempted here.

Figure 2 shows the radial dependence of the fluid rotation vector. The shear in the basic flow is due to viscous corrections to the solution of the inviscid equation, which

https://doi.org/10.1017/jfm.2013.68 Published online by Cambridge University Press

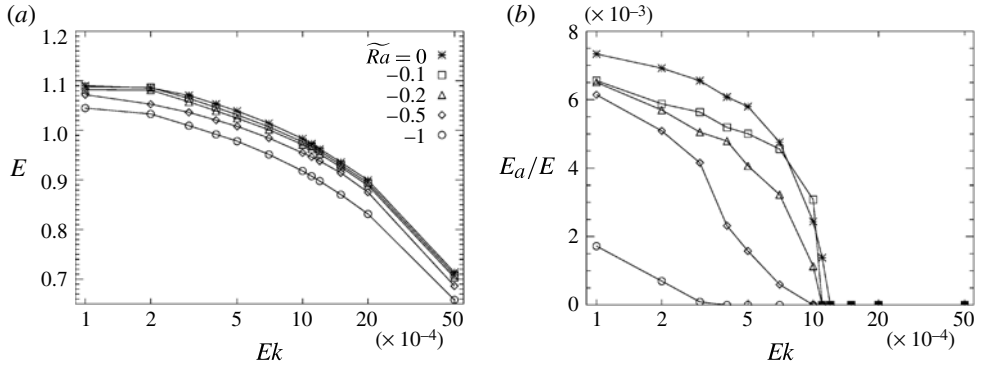


FIGURE 1. Stably stratified precessional flow at Poincaré number $Po = -0.3$. (*a*) The total kinetic energy E and (*b*) the ratio of instability energy E_a to total energy E, as functions of Ekman number Ek at different Rayleigh numbers $\widetilde{Ra}$.

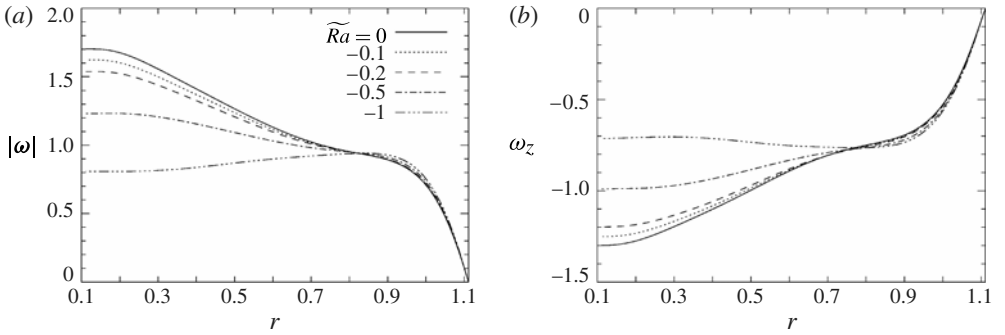


FIGURE 2. Stably stratified precessional flow. Radial dependence of fluid rotation vector at Ekman number $Ek = 2 \times 10^{-3}$ and Poincaré number $Po = -0.3$. (*a*) Modulus $|\boldsymbol{\omega}|$ and (*b*) the z component ω_z.

is simply a solid-body rotation. Viscosity introduces Ekman pumps and shear layers crossing the entire fluid volume, all of which possess a radial velocity component. Since stratification suppresses radial motion, it also reduces the shear. In addition to the modulus of the fluid rotation vector, we also calculated the angle γ between the fluid rotation vector and its average, $\gamma = \arccos(\boldsymbol{\omega} \cdot \overline{\boldsymbol{\omega}}/(|\boldsymbol{\omega}||\overline{\boldsymbol{\omega}}|))$, and γ is less than about 10° in the interior and reaches around 30° near the boundary. Moreover, it is interesting that figure 2(*b*) indicates a counter-rotation of the fluid in the precession frame ($\omega_z + 1 < 0$), which is located in the vicinity of the inner boundary.

The orientation of the fluid rotation axis is best characterized in the precession frame in which the geographic and precession axes are stationary. Figure 3 shows the angle formed by the rotation axis of the fluid (averaged over the fluid volume) with the geographic axis (figure 3*a*) and with the meridian of the precession axis (figure 3*b*) in the precession frame. Figure 3(*a*) parallels the total kinetic energy shown

https://doi.org/10.1017/jfm.2013.68 Published online by Cambridge University Press

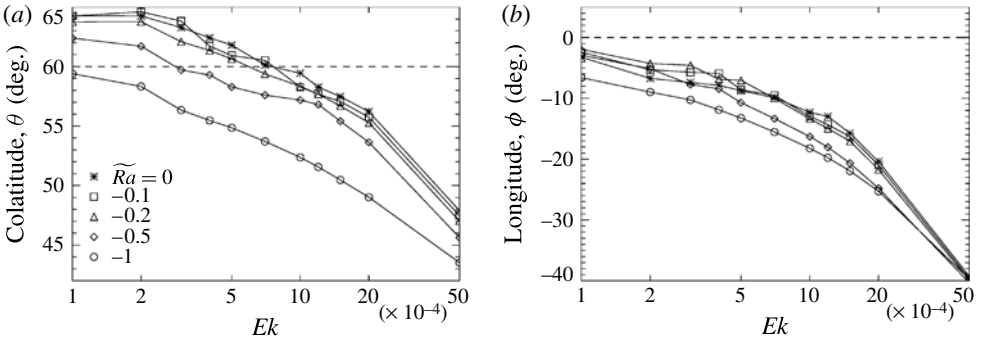


FIGURE 3. Stably stratified precessional flow at Poincaré number $Po = -0.3$. Position of fluid rotation axis as a function of Ekman number Ek at different Rayleigh numbers $\widetilde{Ra}$. (a) Colatitude and (b) longitude of fluid rotation axis in the precession frame. The dashed line denotes the position of the precession axis.

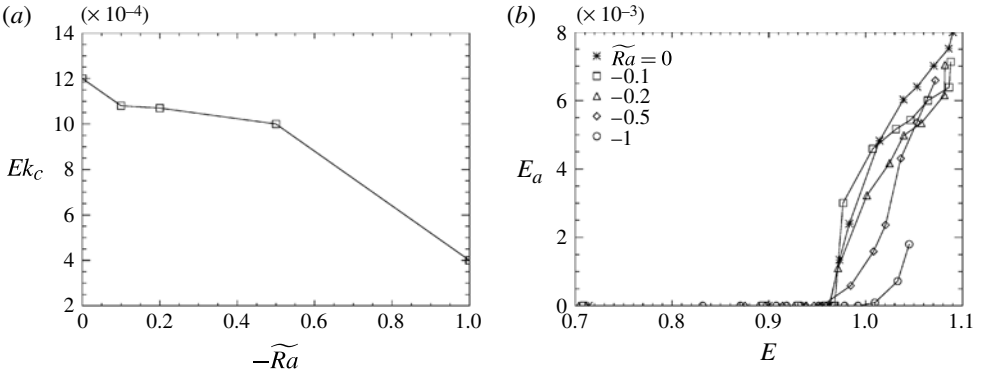


FIGURE 4. Stably stratified precessional flow at Poincaré number $Po = -0.3$. (a) The squares show points determined numerically to lie on the stability limit. The points are connected by a line to guide the eye. (b) The instability energy E_a as a function of the total energy E for different Rayleigh numbers $\widetilde{Ra}$.

in figure 1(a), since the kinetic energy increases with the increasing angle between the fluid and boundary rotation axes. The key point in figure 3(a) is that the stable stratification does not noticeably modify the rotation axis until $\widetilde{Ra} = -1$, and therefore we may conclude that a stable stratification takes effect on the precessional flow only for $|\widetilde{Ra}| > 1$.

The energy in the unstable modes is shown in figure 1(b). Values $E_a \neq 0$ indicate instability. The onset of instability is shifted towards smaller Ek if $|\widetilde{Ra}|$ is increased. This can be seen in more detail in figure 4(a), which shows the critical Ekman number below which the flow is unstable, as a function of $\widetilde{Ra}$. The critical Ekman number decreases monotonically with increasing $|\widetilde{Ra}|$. Even though this is intuitive

https://doi.org/10.1017/jfm.2013.68 Published online by Cambridge University Press

(because stable stratification suppresses radial motion and hence retards the onset of instability), the opposite could have happened as well if the changes in frequency of the inertial modes due to stratification had brought a combination of them closer to a triad resonance. There is an indication of this effect at finite amplitude, since the hierarchy among the different $\widetilde{Ra}$ is not preserved in figure 1(*b*) at $Ek = 10^{-3}$.

The onset of the instability is to a large degree just a matter of the energy in the basic flow. The growth rate of a triad resonance depends on the shear in the basic flow, which increases with the energy of the basic flow. This point is demonstrated in figure 4(*b*), which shows that the onsets of instability for different $\widetilde{Ra}$ nearly coincide if E_a is plotted as a function of E, with the exception of $\widetilde{Ra} = -1$. This again shows that stable stratification is significant only for $|\widetilde{Ra}| = 1$ or larger.

4. Unstably stratified precessional flow

For the study of the fluid core of most planets, it is probably more relevant to investigate the interaction of unstable stratification with precession. In Le Bars & Le Dizés (2006) the geometry of an infinitely long cylinder with an elliptical cross-section was analytically investigated, and it was shown that the elliptical instability and the convective instability may either stabilize or destabilize each other in different parameter regimes. In this section we numerically calculate unstably stratified precessional flow in spherical geometry to study the interaction of precession with unstable stratification.

We select two Ekman numbers, $Ek = 5 \times 10^{-3}$ and 1×10^{-3}, such that the purely precessional flow is stable, namely it is stable at least until $|Po| = 1$ for $Ek = 5 \times 10^{-3}$ and $|Po| = 0.3$ for $Ek = 1 \times 10^{-3}$. Then we test various combinations of Po and $\widetilde{Ra}$ to seek the neutral stability curves of the critical Rayleigh number $\widetilde{Ra}_c$ against $|Po|$ at both Ekman numbers, as well as to calculate some supercritical flows at $Ek = 5 \times 10^{-3}$. The value $\widetilde{Ra}_c$ is sought by increasing or decreasing $\widetilde{Ra}$ in steps of 0.01 at a given Po. We distinguish two different types of flows by the dominant azimuthal wavenumbers in the spectra of the velocity field. These spectra are computed in a frame of reference in which the axes of precession and boundary rotation are stationary and a z'-axis is pointing along the rotation axis of the fluid. The azimuthal angle ϕ' is measured around the z'-axis and the azimuthal wavenumbers are denoted by m'. The onset of convection occurs at $m' = 3$, so that we call the flow 'convective' if the kinetic energy is concentrated at $m' = 3$. If, on the contrary, the spectrum has its largest contributions at $m' < 3$, we call the flow 'precessional'. Flows undergoing precessional instability have their kinetic energy concentrated in these wavenumbers. The motion with wavenumbers $m' = 1$ and 2 can be identified as two inertial modes by the same technique as used by Lorenzani & Tilgner (2001). These two modes, together with the spin-over mode, fulfil the requirements of a triad resonance. Their parameters (latitudinal wavenumber l' and frequency ϖ') are close to two analytically determined eigenmodes with $m' = 1$, $l' = 6$, $\varpi' = -0.537$ and $m' = 2$, $l' = 6$, $\varpi' = -1.093$ (Greenspan 1968).

Figure 5(*a*) shows an approximative stability diagram of unstably stratified precessional flows at $Ek = 5 \times 10^{-3}$. The solid line denotes the neutral stability curve above (below) which flow is unstable (stable), the circles denote the convective flows and the squares the precessional flows. In the absence of precession ($Po = 0$), $\widetilde{Ra}_c$ for the onset of convective instability is 0.45 and the dominant mode is $m' = 3$. When $|Po|$ increases to 0.1, $\widetilde{Ra}_c$ decreases and the instability is still convective. The instability

https://doi.org/10.1017/jfm.2013.68 Published online by Cambridge University Press

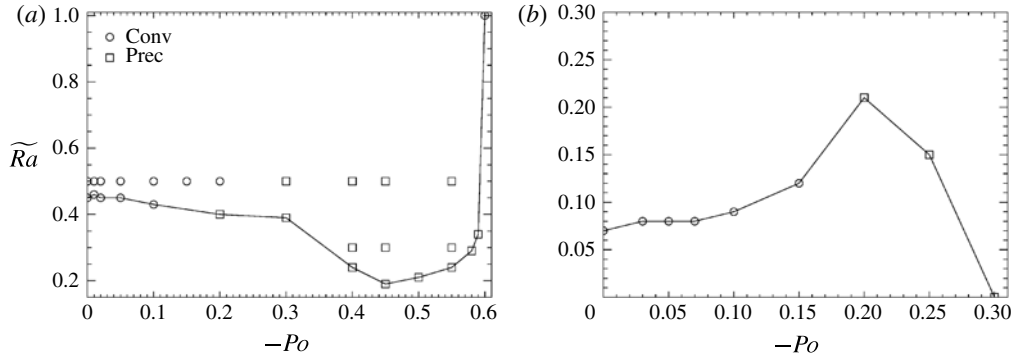


FIGURE 5. Diagram of convective stability and precessional stability for unstably stratified flow at (*a*) $Ek = 5 \times 10^{-3}$ and (*b*) $Ek = 1 \times 10^{-3}$. Points on the solid line denotes points on the neutral stability curve. The circles denote the convective flows and the squares the precessional flows.

becomes precessional for $|Po| = 0.2$ or larger. We see that $\widetilde{Ra}_c$ decreases until it reaches a minimum of $\widetilde{Ra}_c = 0.19$ at $|Po| = 0.45$. The flow becomes more stable with stronger precession for $|Po| > 0.45$. At $|Po| = 0.6$ the flow is so stable that $\widetilde{Ra}_c$ reaches 1. At such a high $\widetilde{Ra}$, the flow pattern is convective again.

Precession has apparently a dual role. On the one hand, both precession and convection can lead to instabilities on their own, so that a superposition of both can be expected to be even less stable. This is observed in figure 5(*a*) around $-Po \approx 0.45$, where the critical Rayleigh number is reduced by more than a factor of 2 by precession, but precession alone in the isothermal fluid (corresponding to $\widetilde{Ra} = 0$) is stable. On the other hand, precession introduces shear on top of the global rotation, and the onset of convective instability has now to be computed for a sheared basic flow, which can lead to a higher Rayleigh number. An example of this phenomenon is seen in figure 5(*a*) for $-Po$ around 0.6.

We then investigate the lower Ekman number of $Ek = 1 \times 10^{-3}$. We only seek the neutral stability curve, but do not calculate any supercritical flows, and we calculate until $|Po| = 0.3$, beyond which the purely precessional flow ($\widetilde{Ra} = 0$) is already unstable (figure 1*b*). Figure 5(*b*) shows this neutral stability curve. As in figure 5(*a*) the circles denote the convective instability and the squares the precessional instability. For purely convective flows ($Po = 0$), the critical Rayleigh number $\widetilde{Ra}_c = 0.07$ at $Ek = 1 \times 10^{-3}$ is much lower than $\widetilde{Ra}_c = 0.45$ at $Ek = 5 \times 10^{-3}$. This is consistent with the asymptotic scaling law of previous calculations (Roberts 1968; Busse 1970; Zhang, Liao & Busse 2007) and numerical calculations (Tilgner & Busse 1997; Zhang *et al.* 2007). Note that the definition of Ra in Tilgner & Busse (1997) should be translated to our definition (2.8) such that the asymptotic scaling law is $\widetilde{Ra}_c = O(Ek^{2/3})$ (this scaling law does not hold precisely in our numerical calculations because we choose too high Ekman numbers). For $Ek = 1 \times 10^{-3}$, $\widetilde{Ra}_c$ has a maximum value of $\widetilde{Ra}_c = 0.21$ at $|Po| = 0.2$, which shows that precession stabilizes the flow at small $|Po|$ whereas it destabilizes the flow at large $|Po|$. We know that the neutral stability curve at $Ek = 5 \times 10^{-3}$ (figure 5*a*) eventually decreases when $|Po|$ is large enough for precession alone to be unstable. In summary, at both the high and low

https://doi.org/10.1017/jfm.2013.68 Published online by Cambridge University Press

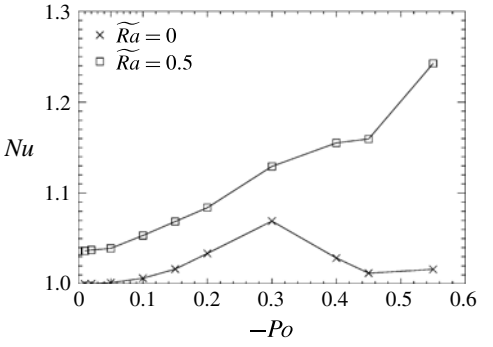


FIGURE 6. Nusselt number Nu at the outer boundary as a function of Po at Ekman number $Ek = 5 \times 10^{-3}$ and Rayleigh numbers $\widetilde{Ra} = 0$ and 0.5.

Ekman numbers, the neutral stability curve is not monotonic but it has a minimum at the high Ek and a maximum at the low Ek.

To end this section we discuss the Nusselt number Nu, which measures the ratio of the total heat transfer to the thermal conduction in the fluid at rest. The stratifying linear temperature profile assumed here is maintained by a heat source so that the Nusselt number depends on radius. The Nusselt number is conveniently computed at the boundaries as

$$Nu = \frac{\langle \partial T/\partial r \rangle}{\Delta T/d}. \tag{4.1}$$

The angular brackets denote an average over the spherical surface of radius r_o or r_i and time. Because of the internal heat source, the Nusselt numbers at the two boundaries are related through

$$Nu|_{r=r_o} - \eta^2 Nu|_{r=r_i} = 1 - \eta^2, \tag{4.2}$$

where $\eta = r_i/r_o = 0.1$ is the aspect ratio used in our calculations. It is verified by our numerical calculations that (4.2) holds precisely. Since Nu at the inner boundary can be deduced from the one at the outer boundary, we only show Nu at the outer boundary. Figure 6 shows Nu at the outer boundary against Po at $Ek = 5 \times 10^{-3}$ for $\widetilde{Ra} = 0$ and $\widetilde{Ra} = 0.5$. Because a purely precessional flow ($\widetilde{Ra} = 0$) has some poloidal component, it also transfers heat, in which case the temperature deviation is a passive scalar. Figure 6 contains several points with Nu around 1.05, which are compared in table 1. At equal poloidal kinetic energy, one flow may be more efficient at transporting heat than the other because of a better correlation between radial velocity and temperature. According to this criterion, convection is more efficient than precession at advecting heat. Adding precession to a convective flow reduces this correlation by a factor of $\sim$4, as shown in table 1.

5. Discussion

We investigated the interaction of precession with thermal stratification. The heat transport in precessional flow is less than in convective flow at equal root mean square of the radial velocity component because of the smaller correlation between

https://doi.org/10.1017/jfm.2013.68 Published online by Cambridge University Press

$\widetilde{Ra}$	Po	Nu	$\langle \int u_r \Theta \, \mathrm{d}V \rangle$	$\langle \int u_r^2 \, \mathrm{d}V \rangle$	$\langle \int \Theta^2 \, \mathrm{d}V \rangle$	$\dfrac{\langle \int u_r \Theta \, \mathrm{d}V \rangle}{\sqrt{\langle \int u_r^2 \, \mathrm{d}V \rangle \langle \int \Theta^2 \, \mathrm{d}V \rangle}}$
0	−0.1	1.006	6.08×10^{-4}	3.81×10^{-3}	4.22×10^{-3}	0.151
0	−0.2	1.034	2.57×10^{-3}	1.33×10^{-2}	1.91×10^{-2}	0.161
0	−0.3	1.069	4.24×10^{-3}	1.50×10^{-2}	2.76×10^{-2}	0.209
0	−0.4	1.029	2.07×10^{-3}	4.78×10^{-3}	1.10×10^{-2}	0.285
0.5	0	1.036	2.04×10^{-3}	4.73×10^{-4}	1.29×10^{-2}	0.826
0.5	−0.1	1.053	3.07×10^{-3}	4.60×10^{-3}	2.07×10^{-2}	0.315
0.5	−0.2	1.084	4.81×10^{-3}	1.56×10^{-2}	3.40×10^{-2}	0.209

TABLE 1. Correlations $\langle \int u_r \Theta \, \mathrm{d}V \rangle$, $\langle \int u_r^2 \, \mathrm{d}V \rangle$ and $\langle \int \Theta^2 \, \mathrm{d}V \rangle$ of purely precessional and convective flows. The angular brackets denote the time average. The first four flows at $\widetilde{Ra} = 0$ are precessionally stable, and the next three flows at $\widetilde{Ra} = 0.5$ are convectively unstable, as shown in figure 5(*a*).

radial velocity and temperature. Unstable stratification together with precession can be either more stable or more unstable than the stratification or precession acting alone. The same could have been expected from the combination of precession with stable stratification, but in this case we only found examples in which the stratification stabilizes the flow. The presence of stable stratification becomes relevant for precession if the ratio of the Brunt–Väisälä frequency to the rotation frequency is near 1.

We present a rough estimate to determine what this criterion implies for various celestial bodies. Consider the extreme case of a body that has cooled down so much that it is nearly isothermal. Within the Boussinesq approximation used here, this corresponds to a stable stratification with a temperature gradient equal to the adiabatic gradient, given by

$$\left(\frac{\partial T}{\partial z} \right)_{ad} = -\frac{g \alpha T}{c_p}, \tag{5.1}$$

where g is the gravitational acceleration, α is the thermal expansion coefficient and c_p is the specific heat capacity at constant pressure. The gravitational acceleration at the surface of a sphere with radius R is given by

$$g = \tfrac{4}{3} \pi G \rho R, \tag{5.2}$$

where G is the gravitational constant. The Brunt–Väisälä frequency for the cooled body under consideration is given by

$$N = \sqrt{-g\alpha \left(\frac{\partial T}{\partial z} \right)_{ad}} = g\alpha \sqrt{\frac{T}{c_p}} = \frac{4}{3} \pi G \rho \alpha R \sqrt{\frac{T}{c_p}}. \tag{5.3}$$

If we accept the following values to be representative of planetary cores,

$$\rho = 11\,390 \text{ kg m}^{-3}, \quad \alpha = 1.5 \times 10^{-5} \text{ K}^{-1}, \quad T = 4000 \text{ K}, \quad c_p = 860 \text{ J kg}^{-1} \text{ K}^{-1}, \tag{5.4}$$

we obtain

$$N = 1.03 \times 10^{-10} R \text{ m}^{-1} \text{ s}^{-1}. \tag{5.5}$$

https://doi.org/10.1017/jfm.2013.68 Published online by Cambridge University Press

If we take as an example planetesimals with a typical radius of $R = 10$ km or $R = 100$ km, we find $N = 10^{-6}$ s^{-1} or $N = 10^{-5}$ s^{-1}, respectively. The rotation of planetesimals has a typical period of $\sim$10 h (Weiss *et al.* 2008), i.e. the rotation rate is $\Omega = 1.7 \times 10^{-4}$ s^{-1}, which implies that the buoyancy is negligible in this context. The situation is different for the Earth, with a core of radius 3.4×10^6 m and a rotation period of 24 h. A stabilizing stratification with a gradient 4 % less than the adiabatic gradient would be enough for the stratification to significantly influence the flow driven by precession.

References

BULLARD, E. C. 1949 The magnetic field within the Earth. *Proc. R. Soc.* A **197**, 433–453.

BUSSE, F. H. 1968 Steady fluid flow in a precessing spheroidal shell. *J. Fluid Mech.* **33**, 739–751.

BUSSE, F. H. 1970 Thermal instabilities in rapidly rotating systems. *J. Fluid Mech.* **44**, 441–460.

BUSSE, F. H. 2000 Homogeneous dynamos in the planetary cores and in the laboratory. *Annu. Rev. Fluid Mech.* **32**, 383–408.

DWYER, C. A., STEVENSON, D. J. & NIMMO, F. 2011 A long-lived lunar dynamo driven by continuous mechanical stirring. *Nature* **479**, 212–215.

GREENSPAN, H. P. 1968 *The Theory of Rotating Fluids*, 1st edn. Cambridge University Press.

JONES, C. A. 2011 Planetary magnetic fields and fluid dynamos. *Annu. Rev. Fluid Mech.* **43**, 583–614.

KERSWELL, R. 1993 Elliptical instabilities of stratified hydromagnetic waves. *Geophys. Astrophys. Fluid Dyn.* **71**, 105–143.

KERSWELL, R. 1995 On the internal shear layers spawned by the critical regions in oscillatory Ekman boundary layers. *J. Fluid Mech.* **298**, 311–325.

LE BARS, M. & LE DIZÉS, S. 2006 Thermo-elliptical instability in a rotating cylindrical shell. *J. Fluid Mech.* **563**, 189–198.

LE BARS, M., WIECZOREK, M. A., KARATEKIN, O., CÉBRON, D. & LANEUVILLE, M. 2011 An impact-driven dynamo for the early Moon. *Nature* **479**, 215–218.

LORENZANI, S. & TILGNER, A. 2001 Fluid instabilities in precessing spheroidal cavities. *J. Fluid Mech.* **447**, 111–128.

LORENZANI, S. & TILGNER, A. 2003 Inertial instabilities of fluid flow in precessing spheroidal shells. *J. Fluid Mech.* **492**, 363–379.

MALKUS, V. R. 1968 Precession of the Earth as the cause of geomagnetism. *Science* **160**, 259–264.

NOIR, J., BRITO, D., ALDRIDGE, K. & CARDIN, P. 2001 Experimental evidence of inertial waves in a precessing spheroidal cavity. *Geophys. Res. Lett.* **28**, 3785–3788.

POINCARÉ, H. 1910 Sur la précession des corps déformables. *Bull. Astron.* **27**, 321–356.

ROBERTS, P. H. 1968 On the thermal instability of a rotating-fluid sphere containing heat sources. *Phil. Trans. R. Soc. Lond.* A **263**, 93–117.

ROBERTS, P. H. & GLATZMAIER, G. A. 2000 Geodynamo theory and simulations. *Rev. Mod. Phys.* **72**, 1081–1123.

TILGNER, A. 1999*a* Magnetohydrodynamic flow in precessing spherical shells. *J. Fluid Mech.* **379**, 303–318.

TILGNER, A. 1999*b* Spectral methods for the simulation of incompressible flows in spherical shells. *Intl J. Numer. Meth. Fluids* **30**, 713–724.

TILGNER, A. 2005 Precession driven dynamo. *Phys. Fluids* **17**, 034104.

TILGNER, A. & BUSSE, F. H. 1997 Finite-amplitude convection in rotating spherical fluid shells. *J. Fluid Mech.* **332**, 359–376.

TILGNER, A. & BUSSE, F. H. 2001 Fluid flows in precessing spherical shells. *J. Fluid Mech.* **426**, 387–396.

VANYO, J. & LIKINS, P. 1971 Measurement of energy dissipation in a liquid-filled, precessing, spherical cavity. *Trans. ASME: J. Appl. Mech.* **38**, 674–682.

https://doi.org/10.1017/jfm.2013.68 Published online by Cambridge University Press

WEISS, B. P., BERDAHL, J. S., TANTON, L. E., STANLEY, S., LIMA, E. A. & CARPORZEN, L. 2008 Magnetism on the angrite parent body and the early differentiation of planetesimals. *Science* **322**, 713–716.

WICHT, J. & TILGNER, A. 2010 Theory and modelling of planetary dynamos. *Space Sci. Rev.* **152**, 501–542.

ZHANG, K., LIAO, X. & BUSSE, F. H. 2007 Asymptotic solutions of convection in rapidly rotating no-slip spheres. *J. Fluid Mech.* **578**, 371–380.

https://doi.org/10.1017/jfm.2013.68 Published online by Cambridge University Press